*Present address: Dépt. de Physique Nucléaire et Corpusculaire, Université de Genève, Geneva, Switzerland.
†Present address: CERN, 1211 Geneva 23, Switzerland.
‡Research supported by the United States Atomic Energy Commission under Contract No. AT(11-1).
§Operated by Universities Research Association, Inc. under contract with the United States Atomic Energy Commission.
‖Work supported by the United States Atomic Energy Commission.
¶Present address: Brookhaven National Laboratory, Upton, New York 11973.
**Present address: Bell Laboratories, Holmdell, New Jersey 07733.
††Work supported in part by the National Science Foundation.

[1]V. Hungerbühler *et al.*, Nucl. Instrum. Methods 115, 221 (1974).
[2]W. J. Willis *et al.*, Nucl. Instrum. Methods 91, 33 (1971).
[3]With an index of refraction of 1.000 516.
[4]R. T. Deck, Phys. Rev. Lett. 13, 169 (1964).
[5]V. Hungerbühler *et al.*, Phys. Rev. Lett. 24, 1234 (1973).
[6]W. Tanenbaum *et al.*, Phys. Rev. Lett. 33, 175 (1974).
[7]A. L. Kane, Acta Phys. Pol. B3, 845 (1972).
[8]H. J. Lipkin, Phys. Rev. D 7, 846 (1973).
[9]Brandeis-Maryland-Syracuse-Tufts Collaboration, in *Hyperon Resonances 70:* Proceedings of 1970 Duke Conference, edited by E. C. Fowler (Moore, Durham, N. C., 1970), p. 317.

PHYSICAL REVIEW D VOLUME 10, NUMBER 7 1 OCTOBER 1974

$\pi^+\pi^+ \to \pi^+\pi^+$ scattering below 0.7 GeV from $\pi^+p \to \pi^+\pi^+n$ at 5 GeV/c

J. P. Prukop, O. R. Sander, J. A. Poirier, C. A. Rey, A. J. Lennox, B. C.-j. Chen, N. N. Biswas, N. M. Cason, V. P. Kenney, and W. D. Shephard
*Department of Physics, University of Notre Dame, Notre Dame, Indiana 46556**

R. D. Klem and I. Spirn
Argonne National Laboratory, Argonne, Illinois 60439†
(Received 22 April 1974)

Magnetostrictive spark chambers were used with a large magnet spectrometer to study the reaction $\pi^+p \to \pi^+\pi^+n$ at 5.0 GeV/c at Argonne National Laboratory. We measured differential cross sections for this reaction in the region of low nucleon momentum transfer and by extrapolation obtained cross sections and phase shifts for the reaction $\pi^+\pi^+ \to \pi^+\pi^+$ in the region of dipion mass less than 0.7 GeV. Effects of the interference between the strong $\pi^+\pi^+$ amplitude and the Coulomb amplitude off the mass shell were investigated and were found to be small. The S-wave phase shifts for $\pi^+\pi^+$ scattering near threshold were parameterized in terms of a scattering length, a_2, and an effective range, r_2; the D wave by a scattering parameter, b_2. The fits obtained by extrapolation techniques were insensitive to b_2 and gave $a_2 = -0.24 \pm 0.02$ F and $r_2 = -1.0 \pm 1.7$ F, where the error quoted is statistical. The fits obtained by off-shell fitting gave $a_2 = -0.22 \pm 0.04$ F, $r_2 = -0.34^{+0.9}_{-1.2}$ F, and $b_2 = -0.0041^{+0.0025}_{-0.0021}$ F[5]. These results for a_2 are inconsistent with a number of theoretical calculations.

I. INTRODUCTION

The scattering of pions from pions is the simplest example of a strong interaction amplitude and is, therefore, very fundamental. Its simplicity is due in part to the facts that the pion has no spin, obeys Bose-Einstein statistics, has a short-range force, and at low energy has but few partial waves. Because of the light mass of the pion it has the longest range of the hadrons and thus the one-pion-exchange mechanism dominates in many reactions. Thus an understanding of the $\pi\pi$ interaction is important not only in itself but for the understanding of many other reactions as well. The $\pi^+\pi^+$ interaction is particularly simple because it is in the pure isotopic spin state $I=2$ and is not complicated by the presence of inelastic channels for energies less than four times the pion mass.

As there is at present no direct way to study the $\pi^+\pi^+$ interaction, we have chosen to explore the dipion system in the reaction $\pi^+p \to \pi^+\pi^+n$. By assuming the dominance of the one-pion-exchange mechanism (OPE) the $\pi^+p \to \pi^+\pi^+n$ cross section is related to the cross section for the scattering of a beam pion by the exchanged pion. The exchanged (virtual) pion is off the mass shell by an amount $\Delta^2 + \mu^2$, where μ is the pion rest mass and Δ^2 is the square of the momentum transfer between the incoming proton and outgoing neutron. The $\pi^+\pi^+$

cross section obtained by extrapolating from off-shell to on-shell values for the exchanged pion mass was used to obtain the $\pi^+\pi^+$ phase shifts for S-wave scattering. The phase shifts for D-wave scattering were determined from the angular distributions. These phase shifts involve only the pure $I=2$ isotopic spin state. Thus, a determination of their values is particularly useful in the study of other reactions, such as $\pi^-\pi^+ \to \pi^-\pi^+$, $\pi^-\pi^+ \to \pi^0\pi^0$, and $\pi^\pm\pi^0 \to \pi^\pm\pi^0$, which contain various mixtures of the $I=0$, $I=1$, and $I=2$ states. Furthermore, our phase shifts were obtained from dipion systems in the low-mass region where various theories have described properties of $\pi\pi$ scattering. In particular, the threshold behavior of $\pi\pi$ scattering has been parameterized in terms of scattering lengths. Our results include a determination of these parameters for the $I=2$, $\pi^+\pi^+$ state. The necessary data on the $\pi^+p \to \pi^+\pi^+n$ interactions at 5.03 GeV/c were obtained in a magnetostrictive spark chamber experiment at Argonne National Laboratory and had a statistical accuracy of ~60 events/μb near threshold.

Some of the other physics variables used in the calculation of the cross sections and phase shifts are the invariant dipion mass, $M_{\pi\pi}$; the angle, θ_J, between the incident and outgoing pion in the dipion rest frame; and the angle, ϕ_{TY}, between the nucleon scattering plane and the dipion decay plane (Treiman-Yang angle). The momentum transfer between the incoming and outgoing pion is the Mandelstam variable, t, which is linearly related to $\cos\theta_J$. The experiment was designed to obtain data in the following kinematic regions: $M_{\pi\pi} < 0.7$ GeV, $\Delta^2 < 8\mu^2$, and for all values of ϕ_{TY} and θ_J. The spectrometer system kinematically eliminated the $\pi^+p \to \pi^+p$ reaction and provided $\pm 0.5\%$ momentum determination with better than one milliradian angular resolution. This resolution was sufficient to eliminate most of the background contamination from the reaction $\pi^+p \to \pi^+p\pi^0$. The trigger included no beam veto counter and no neutron detectors which might have introduced experimental biases in Δ^2 and $\cos\theta_J$. We were thus able to extrapolate in Δ^2 and fit the data in the low-t regions of the dipion system.

II. EXPERIMENTAL EQUIPMENT

The plan view of the experiment is shown in Fig. 1. We chose a right-handed coordinate system with the X axis in the direction of the beam. The origin of the system was at the center of the magnet with the Z axis up and the Y axis horizontal.

The pion beam was produced at the Argonne National Laboratory Zero Gradient Synchrotron and had about $\pm 0.5\%$ momentum spread at 5.03 ± 0.03 GeV/c. The spot size (half width at half maximum) was ± 5 mm vertical and ± 4 mm horizontal with ± 7.5 mrad and ± 10 mrad divergences, respectively. The ratio of pions to protons was ~25%. From the Čerenkov counter pressure curve it was determined that contamination in the beam relative to π^+ was about 2% μ^+, negligible K^+, and $< 0.2\%$ e^+. The Čerenkov counter was >99.8% efficient for selecting pions.

As the major element of our particle spectrometer, we used an SCM-105 magnet with a horizontal aperture of 2.14 m and a vertical aperture of 0.67 m. The central field was 8 kG and the effective length of the field was 1.02 m. A set of magnetic mirrors was installed to shield the magnetostrictive wands on the spark chambers.

We mapped the major component of the magnetic field with a Hall probe. As suggested by Wind[1] we concentrated the major fraction of our measurements on the boundary of the spatial region of interest. Measurements of the minor components were also made in several areas for later comparison with values predicted by a mathematical model of the magnet. This model, similar to that of Highland and Macek,[2] utilizes the physical magnet dimensions and requires relatively few terms, each of which has the correct asymptotic behavior at large distances. The model has explicit formulas for the various components of the magnetic field which intrinsically obey Maxwell's equations. Thus by fitting the major component of the magnetic field one obtains the minor components directly. With the model as described, we succeeded in fitting the measurements of the major component to $\pm 0.4\%$ of the central field and the calculation of the minor components then agreed with the measurements to within $\pm 3\%$. Much of this error was in the original measurements. Final momentum errors on secondary particles due to magnet fitting errors are estimated to be 0.09%.

The trigger for the spark chambers was generated by an array of scintillation counters which were checked throughout the experiment with a Co^{60} source to ensure that their efficiencies remained high. The basic beam telescope required $B1$, $B2$, and the Čerenkov counter, $\check{C}$, to be in coincidence, with A in anticoincidence. Counter A was 254 mm square with a 25.4-mm hole in its center and had photomultipliers attached to two opposite sides to avoid possible dead spots. An inhibit gate, G, was on (a) for ~20 msec after each event to allow the high-voltage pulser time to recharge, (b) for 1 μsec after each beam particle to avoid detecting old beam tracks, and (c) during the time an event was being stored in the

computer. The coincidence of $B1 \cdot B2 \cdot \check{C} \cdot \overline{G}$ was defined as a beam pion, B.

The dE/dx counter, D, was an important element of the event trigger, selecting multiply charged final states and rejecting noninteracting beam particles. It was constructed from 3.2 mm pilot F scintillator and had a sensitive area of 254 mm × 508 mm. Light from each of the four edges was collected by four separate photomultiplier tubes. A uniformity of better than 5% over the active area of this counter was achieved by carefully adjusting the gains of these tubes. As the experiment progressed the counter uniformity was periodically checked by measuring the counting rate from a Co^{60} source placed at various test points on the surface of the counter. The linearly added outputs of the four photomultipliers were discriminated so that the counting rate on beam particles was ~10%. This system was regularly checked for drift. A detailed Monte Carlo calculation using correct Landau straggling and photon statistics for our light pipes and photomultipliers showed that 6% of the events were lost when the dE/dx discriminator was set as above.[3]

The hodoscope was designed by orbiting Monte Carlo events of the type $\pi^+p \to \pi^+\pi^+n$ through a magnetic field and noting where the two pions crossed the hodoscope plane. Since the trigger would require two charged particles in the hodoscope, it was necessary to minimize the chance that both would go through the same counter. The final design incorporated 12 counters, each 102 mm × 457 mm, to cover the central region ($|Y| \leq 306$ mm and $|Z| \leq 457$ mm) and six large full length counters to cover the region 306 mm $< |Y| <$ 1118 mm. The smooth acceptance at low $M_{\pi\pi}$ and low Δ^2 that was achieved is detailed later. The hodoscope counters were each discriminated, and these unit height pulses were linearly added. In the trigger the resulting pulse, H, was required to have a height ≥ 2.

In summary, the event trigger, EVT, was $B \cdot \overline{A} \cdot D \cdot H(\geq 2)$. We also scaled A, B, $B \cdot \overline{A}$, $B \cdot \overline{A} \cdot D$, EVT, SEM2 (a secondary emission beam monitor), and the number of beam pulses. Target full ratios, such as $B \cdot \overline{A}/EVT \sim 100$, $B \cdot \overline{A}/B \cdot \overline{A} \cdot D \sim 6$, and $B \cdot A/B \sim 0.86$, were used to monitor the trigger and beam.

The hydrogen target was 152 mm long and had only 0.5 mm of Mylar and superinsulation in the beam at each end. The target length was kept short and the dE/dx counter was constructed of thin scintillator in order to minimize the effects of multiple scattering (less than 0.8 milliradians, rms).

The logic event trigger was applied to two thyristor arrays, each of which provided an 800-volt, 100-nsec pulse with 20 nsec delay and 10 nsec rise time into two parallel 50-ohm lines to drive two thyratron trigger grids. These thyratrons produced a 40-nsec rise time, 4–5-kilovolt, 200-nsec square pulse by discharging a coaxial cable which was used for energy storage.

Each chamber consisted of four planes, two inner coordinate planes crossed at angles to each other (either perpendicular or ±15° from the vertical) and two outer parallel planes of horizontal wires which electrically formed a strip transmission line of ~4 ohms impedance. However,

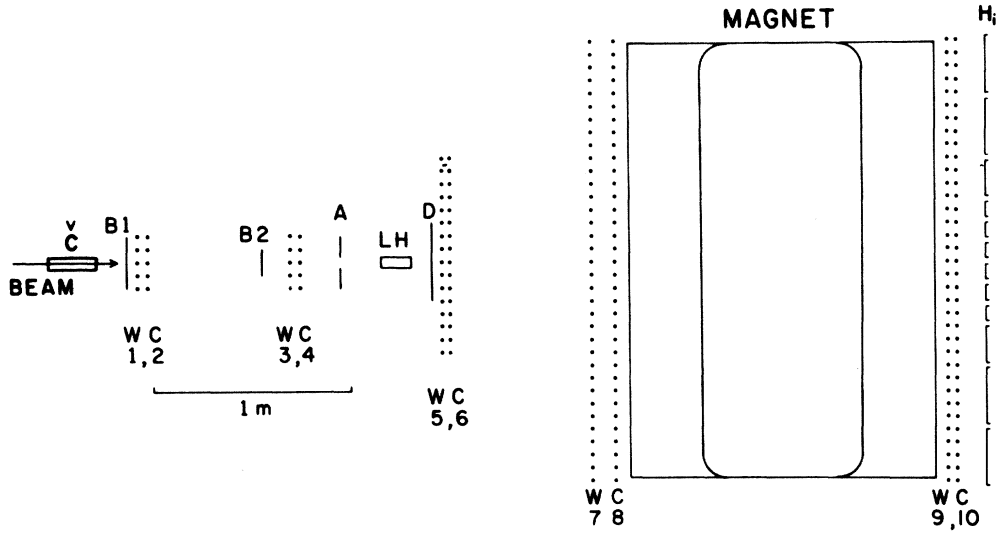

FIG. 1. Over-all plan view of the experiment. The dotted lines represent the position of magnetostrictive wire spark chambers, WC. The solid lines represent the locations of the scintillation counters used in the logic which triggered the WC's. The Čerenkov counter, $\check{C}$, is located about 20 m further upstream than indicated.

we fed each chamber with an 8-ohm transmission line and terminated it with 18 ohms on the opposite side. This provided a boost in pulse voltage with little distortion of the rectangular pulse over the entire active area of the chamber. The termination was through three parallel chains of three 18 ohm resistors in series with a 1N3044B Zener diode. During the negative high-voltage pulse this provided the chamber termination. During the pulser recharge time the Zener diodes produced a pulsed 100 volt clearing field. The diodes also presented a high impedance to an adjustable dc clearing field.

The wire planes were supported by G-10 epoxy-glass frames 9.5 mm thick. At the 0.5-kg tension used there was less than 0.1 mm deflection over the 2.13 m length of the largest chamber. The 0.15-mm-diameter aluminum wires had a spacing of 0.5 mm for the inner planes and 1.5 mm for the outer planes. Electrical contact was made using brass bus bars bonded to the aluminum wires with EPO-TEK 417LV silver-loaded conductive epoxy which proved to be suitable for this pulsed high-current application.

In order to resolve ambiguities in Y and Z coordinates for two sparks another coordinate pair, U and V, was provided. This was accomplished for the small and intermediate size chambers by rotating an identical YZ chamber by 45°. For the large chambers near the SCM-105 magnet, the UV information was obtained from chambers with coordinate plane wires placed at ±15° to the vertical.

The spark positions were determined with wands of magnetostrictive wire. The wire was Wilbur Driver Remendur of either 0.15 mm diameter or 0.13 mm × 0.51 mm rectangular cross section and transmitted a longitudinal mode pulse at ~5 mm per μsec. It was threaded through thin-walled Teflon tubing, and copper tape was placed over the wand to provide an image current which enhanced the size of the magnetostrictive pulses. The wands were magnetically biased in the direction of the pulsed magnetic fields from the chamber wires so they would not be demagnetized by the spark current. For chambers near magnets, strips of soft iron were placed over the wands to supplement the magnetic shielding already provided by the magnetic mirrors on the spectrometer magnet. The magnetostrictive pulses were amplified in SAC 1001A preamplifiers before being fed into external amplifiers with variable gain. The effect of 20-MHz clock noise in the SAC 1148 digitizing system was eliminated by feeding the amplified pulses into a comparator before digitizing them. The 1148 digitizer uses the leading edge of a start pulse from a wand to start all scalers associated with a coordinate plane. The leading edge of a data pulse halves the counting rate of its scaler and the trailing edge stops this scaler. Thus the center of a data spark is found. The data were corrected for the fact that the leading edge of the start pulse (and not its center) started the scalers. After all

TABLE I. Summary of all corrections to the cross section.

(a) Inverse of the weighting factors applied on an event-by-event basis.

	Range
1. Geometrical acceptance of apparatus	1.00 to 0.10
2. Interactions of secondary particles	0.98 to 0.90
3. Decay of secondary pions	0.96 to 0.85

(b) Inverse of the weighting factors applied to all events.

	Effect
1. MM^2 and TEUTA χ^2 cuts, background contaminations	$1 - 0.190 \pm 0.020$
2. Cut on CIRCE goodness-of-fit parameter	$1 - 0.030 \pm 0.010$
3. Chamber inefficiencies	$1 - 0.113 \pm 0.012$
4. Spark cut	$1 - 0.296 \pm 0.030$
5. Ambiguities in track reconstruction	$1 - 0.057 \pm 0.020$
6. μ and e contamination	$1 - 0.019 \pm 0.002$
7. dE/dx trigger inefficiency	$1 - 0.060 \pm 0.005$
8. Empty-target effects	$1 + 0.010 \pm 0.005$
9. Beam absorption in hydrogen target	$1 - 0.009 \pm 0.002$
10. Effect of Coulomb scattering	$1 - 0.000 \pm 0.005$
Net effect of over-all systematic corrections	$1 - 0.573 \pm 0.022$

the spark positions were digitized they were transferred from the scalers into the computer.

Start-and-stop fiducial wires were attached to the chambers at surveyed positions. They were excited by the same high-voltage pulse as the wires of the chamber and their pulses were 1 to 3 scaler counts ahead of the actual data pulses due to the spark formation time. In addition, special wires every 100 mm along the wands could be externally excited and coordinated with survey measurements.

A standard 90% neon, 10% helium gas mixture with an adjustable percentage of ethyl alcohol was continuously circulated through the chambers and purification system. The ethyl alcohol usually constituted ~0.4% of the gas and was added by passing 3% of the standard neon-helium mixture through a vessel containing ethanol maintained at 31 °C.

During the 0.5-second beam spill the digitized spark position data in the SAC scalers were transferred to a Varian 620i on-line computer which performed consistency checks and typed appropriate error messages. The raw data were then written on magnetic tape to be later processed off line.

In the time between beam spills the computer displayed the actual spark positions or histograms of spark positions on an oscilloscope. Just before each beam spill, the computer tested the SAC scaler system with a fixed pattern of data to ensure that all channels were operating correctly. The computer also controlled the initiation and termination of data-gathering runs and provided an end-of-run summary. The monitoring of hardware functions by the various consistency tests alerted us to equipment malfunctions. The ability to see the data displayed on-line proved useful in optimizing the experimental conditions.

III. DATA REDUCTION

The track-finding program, CRUNCH, first transformed the raw data from the magnetic tapes into real-space coordinates. Each of the data tapes had a short run made with the logic set to trigger the chambers on noninteracting beam particles. This provided a sample of single beam tracks which could be reconstructed into real-space coordinates by initially using the actual surveyed centers of the chambers. The differences of the data points from the best straight line were used to calculate a corrected center position for the chambers for each data tape. The average value for the scale factors for each plane was also found and was updated constantly to avoid errors due to any overall change in sound velocity in the magnetostrictive wires. This method of chamber locating and scale calibrating ensured the highest reconstruction accuracy. After correcting the nonlinear changes of sound velocity in the wires, the magnetostrictive spark chamber system had an overall spatial positioning accuracy of about 0.5 mm, or an angular resolution of 0.5 mrad.

We required a spark cut of fewer than three sparks in chambers 5 and 6 to enhance the basic trigger requirement that only two-track events

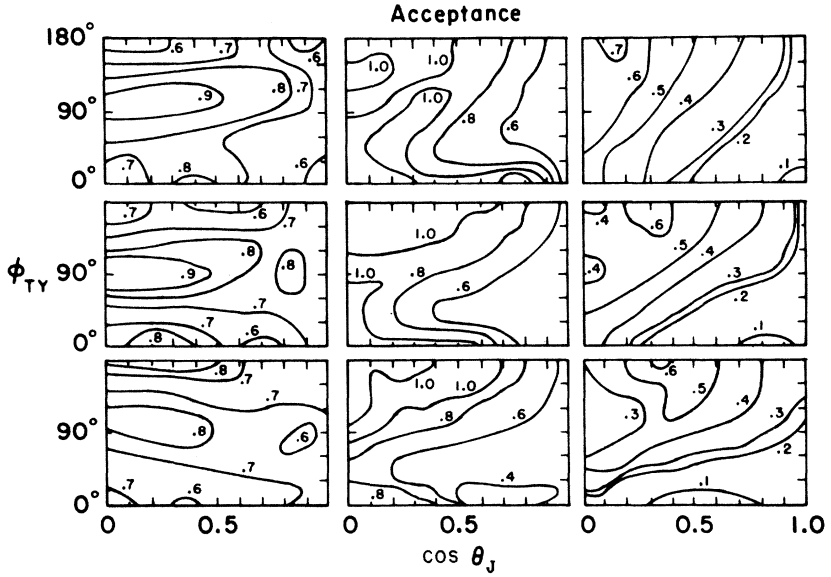

FIG. 2. Contours of constant geometrical acceptance. On each plot the abscissa is $\cos\theta_J$ and the ordinate is ϕ_{TY}. The plots are shown for $M_{\pi\pi}$ fixed at 0.3, 0.5, and 0.7 GeV (left, center, and right columns, respectively), and Δ^2 fixed at $1\mu^2$, $3\mu^2$, and $6\mu^2$ (top, middle, and bottom rows, respectively).

be accepted. Pairs of spark coordinates from UV chambers (UV pairs) were converted to all possible YZ pairs for further processing. The program then found all possible tracks which originated in the target and which entered the magnet in the XY projection. The same procedure was followed for the XZ projection. Then the intersection of each secondary track with the beam track was found. The X values for the vertices calculated in each projection were required to be consistent with each other and to be within ±83 mm of the center of the target (to within 5 standard deviations).

The program then examined the bank of all possible tracks entering the magnet and attempted to associate each track with one or more sparks in the chambers after the magnet. The vertical focusing effect of the fringe field of the magnet was rather severe due to the addition of the magnetic mirrors. A polynomial approximate method was used to account for these effects in the following manner. A grid of momentum vectors was orbited through the magnet and the results were fitted to a polynomial. The number of terms was increased until a good fit was obtained. The difference between Z in chambers 9 or 10 and the straight-line projection of a track entering the magnet was defined as ΔZ; for the XY plane ΔY was defined similarly. For each track the polynomial was evaluated using ΔY and the Y slope and Z position before the magnet. A given Y coordinate was paired with a given Z coordinate to define a position on a specific track only if their corresponding ΔY and ΔZ values were consistent.

The program then attempted to find two tracks with the most complete and consistent information after the magnet. For each track the Y slope before the magnet was compared with possible Y slopes after the magnet; inconsistent data in chambers 9 and 10 were deleted from the data bank. The information defining the most consistent track was set aside and the search was repeated for a second track. When the two best tracks had been found their spark positions were recorded on magnetic tape for processing in the geometrical fitting program.

The geometrical fitting program[4] is an adaptation of the program CIRCE, which was written at SLAC to deal with tracks having an unseen vertex. It mathematically constrains the over-all least-squares fit of the system of tracks to have a common vertex in the hydrogen target. It is also specially adapted to handle very nonuniform magnetic fields.

The kinematic and hypothesis fitting[5] was done by a companion SLAC program called TEUTA, which fitted the hypotheses $\pi^+p \to \pi^+\pi^+n$, $\pi^+p \to \pi^+p$, $\pi^+p \to \pi^+p\pi^0$, and $\pi^+e \to \pi^+e$. The geometry of the spectrometer effectively excluded π^+p elastic events and indeed no such fits were obtained. The total of 54 tapes with data from 3.1 million event triggers were processed by CRUNCH at a rate of 0.02 second per event. The 10^5 surviving events were geometrically reconstructed by CIRCE at two seconds per event, and 60% of these were finally processed by TEUTA at ~0.5 second per event.

IV. DETERMINATION OF THE CROSS SECTION

The weighting factors applied on an event-by-event basis to determine the total number of weighted events entering into the calculation of the $\pi^+p \to \pi^+\pi^+n$ cross sections are summarized in Table I(a). When the net effect of the over-all systematic corrections listed in Table I(b) is applied to the product of the number of beam pions and the number of protons in the target, a final conversion factor of 0.014 μb per weighted event is obtained. Further details of the calculations and considerations leading to the values listed in Table I are given below.

The first step in calculating the geometrical acceptance was to determine which regions in the physics variables had low acceptance. Monte Carlo events generated with various values for the physics variables $M_{\pi\pi}$, Δ^2, ϕ_{TY}, and $\cos\theta_J$ were orbited through an exact representation of our spectrometer and counter arrays. Some of the resulting acceptance contours are shown in Fig. 2. We have only very small areas of low acceptance for the regions of $M_{\pi\pi} < 0.7$ GeV and $\Delta^2 < 8\mu^2$, with no

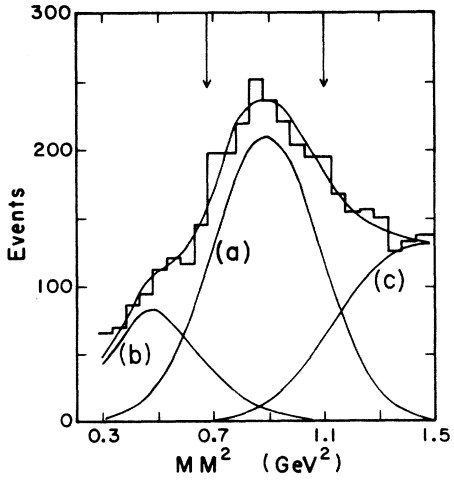

FIG. 3. Maximum-likelihood fits to the MM^2 plot for $\Delta^2 < 8\mu^2$ and $M_{\pi\pi} < 0.7$ GeV. The relative amounts of each reaction inside the indicated cuts are (a) $\pi^+p \to \pi^+\pi^+n$ = 1493 events, (b) $\pi^+p \to \pi^+p\pi^0$ = 123 events, and (c) $\pi^+p \to \pi^+\pi^+n\pi^0$ = 180 events.

regions of zero acceptance (holes). For the region of $M_{\pi\pi} > 0.7$ GeV, the holes that occur in the data first appear for $\cos\theta_J$ near $+1$. For exploring the effects of Coulomb interference, the data are thus less useful above 0.7 GeV. Therefore, we limited the data analysis to the sample where $M_{\pi\pi} < 0.7$ GeV and $\Delta^2 < 8\mu^2$. For the remainder of this paper we confine our discussion to this kinematic region.

Rather than generate the exact distributions needed to create Monte Carlo events to be used in a detailed calculation of acceptance, we used the actual data events to determine the geometrical weight for each event.[6] Because the beam and target were unpolarized the physics was invariant to a rotation about the incoming pion direction. Furthermore, our experimental apparatus had no regions in the physics variables where all events were excluded. Thus, we were able to generate events having a uniform population about the beam direction by rotating actual data events about this direction. Since we were using actual data events, the acceptance calculation properly reflected the actual vertex locations and beam divergences of the event sample. A weight-generating program rotated each event about the incident pion direction in 100 steps of 3.6°, thus changing the orientation of the events relative to the apparatus without changing the physics variables of the event. Each of the 100 pairs of rotated secondary tracks was orbited through a software representation of the experiment. The geometric acceptance of the event was defined as the percentage of those events where both secondary tracks passed through the magnet and met the triggering requirements. In this software representation the stops were more stringent than the physical magnet dimensions.

TABLE II. $\sigma(\pi^+ p \to \pi^+\pi^+ n)$ in μb per bin.

Edges on $(\Delta')^2$ bins \ Edges on $\cos\theta_J$ bins	0.0	0.1	0.2	0.3	0.4	0.5	0.6	0.7	0.8	0.9	1.0
						$M_{\pi\pi} < 0.5$ GeV					
$0\mu^2$	0.420 ±0.078	0.254 ±0.061	0.313 ±0.068	0.335 ±0.071	0.369 ±0.076	0.453 ±0.084	0.281 ±0.068	0.393 ±0.082	0.630 ±0.112	0.395 ±0.088	
$2\mu^2$	0.279 ±0.065	0.248 ±0.059	0.215 ±0.055	0.445 ±0.084	0.193 ±0.057	0.355 ±0.077	0.242 ±0.064	0.271 ±0.071	0.331 ±0.083	0.433 ±0.100	
$4\mu^2$	0.259 ±0.065	0.439 ±0.080	0.403 ±0.078	0.418 ±0.097	0.447 ±0.092	0.405 ±0.092	0.370 ±0.085	0.192 ±0.063	0.420 ±0.100	0.135 ±0.058	
$8\mu^2$											
						$0.5 < M_{\pi\pi} < 0.6$ GeV					
$0\mu^2$	0.215 ±0.060	0.317 ±0.079	0.434 ±0.091	0.385 ±0.092	0.334 ±0.092	0.289 ±0.089	0.475 ±0.123	0.568 ±0.134	0.517 ±0.145	1.327 ±0.254	
$2\mu^2$	0.279 ±0.075	0.241 ±0.069	0.190 ±0.062	0.241 ±0.076	0.243 ±0.075	0.292 ±0.092	0.268 ±0.111	0.293 ±0.099	0.328 ±0.104	0.616 ±0.179	
$4\mu^2$	0.269 ±0.092	0.592 ±0.131	0.268 ±0.076	0.428 ±0.103	0.255 ±0.076	0.346 ±0.121	0.263 ±0.085	0.309 ±0.107	0.503 ±0.176	0.144 ±0.074	
$8\mu^2$											
						$0.6 < M_{\pi\pi} < 0.7$ GeV					
$0\mu^2$	0.443 ±0.101	0.551 ±0.120	0.308 ±0.093	0.682 ±0.150	0.708 ±0.180	0.480 ±0.141	0.879 ±0.253	1.106 ±0.297	1.133 ±0.302	1.746 ±0.444	
$2\mu^2$	0.269 ±0.087	0.171 ±0.066	0.298 ±0.097	0.524 ±0.180	0.584 ±0.202	0.356 ±0.138	0.225 ±0.120	0.523 ±0.188	0.793 ±0.259	0.576 ±0.230	
$4\mu^2$	0.254 ±0.090	0.504 ±0.148	0.472 ±0.159	0.153 ±0.071	0.332 ±0.102	0.458 ±0.187	0.879 ±0.291	0.628 ±0.237	0.611 ±0.210	0.852 ±0.289	
$8\mu^2$											

Actual data events which did not satisfy these software stops were rejected from the sample. In this way the acceptance was individually calculated for each event to an accuracy of ~1%.

Corrections for strong interactions of secondary particles were minimized because the spark cut in CRUNCH deleted events for which more than two charged particles entered chambers 5 and 6. The probability of losing an event because of secondary interactions which did not produce additional forward charged particles ranged from 2% to 10%. Losses due to the decay of secondary pions ranged from 4% to 15%.

Figure 3 shows the square of the missing mass of the neutrals, MM^2, in a one-constraint analysis. A peak at about 0.88 GeV^2 indicates the presence of reaction (1), $\pi^+p \to \pi^+\pi^+n$. There are events having MM^2 above or below this value which do not have Gaussian distributions. These come from the reaction (2), $\pi^+p \to \pi^+p\pi^0$, on the low side, and from reaction (3), $\pi^+p \to \pi^+\pi^+n\pi^0$, on the high side. In order to study the contaminations from these two backgrounds we first determined their distributions in MM^2. For reaction (2) the shape was found by using a Monte Carlo sample of events as input to the acceptance program. For reaction (3) the shape[7] was assumed to be roughly the same as that of $M^2(\pi_1^-p)$ for the reaction $\pi^-p \to \pi_1^-\pi_2^-\pi^+p$. Using these distributions and assuming a Gaussian shape for MM^2 in reaction (1), we then fitted the observed, unweighted MM^2 distribution and determined the relative contribution from each reaction. The fitted curves are shown in Fig. 3. This information enabled us to determine the effect of the MM^2 cuts indicated by arrows in Fig. 3. An additional cut on P (the kinematic fit probability calculated in TEUTA) requiring the $P(\pi^+\pi^+n)$ be greater than twice $P(\pi^+p\pi^0)$ reduced the contamination due to this background. There is a strong correlation between MM^2 and $P(\pi^+\pi^+n)$; a 1% cut on $P(\pi^+\pi^+n)$ had no additional effect beyond the effect of the MM^2 cut. The effective average overall correction for these cuts and contamination was $(19 \pm 2)\%$. Results of a more detailed study of these effects and their dependence on $M_{\pi\pi}$ and Δ^2 were applied as weighting factors on an event-by-event basis to obtain the cross sections given in Table II.

An additional cut was made on the total χ^2 calculated by CIRCE in fitting the orbits to the spark data. The correction for this cut was 3%.

The efficiency for reconstructing an event is highly dependent on the sensitivity of the track-finder program to missing and extraneous sparks. To estimate this efficiency three separate and exclusive categories were considered: (1) Events lost due to the spark cut in the CRUNCH program; (2) events lost because so many sparks were missing that CRUNCH could not reconstruct the event; and (3) events lost when a combination of missing sparks and extraneous sparks combined to give an erroneous reconstruction.

The spark cut was used to exclude most three charged particle final states. It also excluded good $\pi^+p \to \pi^+\pi^+n$ events whenever an extraneous spark occurred in chambers 5 or 6. In order to determine the size of this loss and calculate the number of good events deleted by the spark cut because of δ-ray and strong secondary interactions,

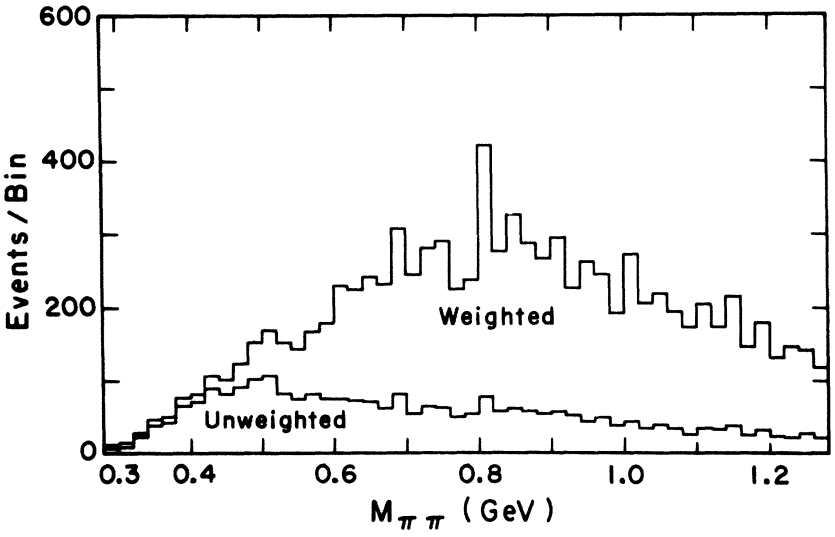

FIG. 4. The 2605 raw or 9411 weighted $\pi^+p \to \pi^+\pi^+n$ data events displayed in $M_{\pi\pi}$ bins of 0.02 GeV. The following cuts have been applied: $0.68 < MM^2 < 1.1$ GeV^2, probability $(\pi^+p \to \pi^+\pi^+n) >$ twice the probability $(\pi^+p \to \pi^+p\pi^0)$, and $(\Delta')^2 < 8\mu^2$. The weighted events with $M_{\pi\pi} < 0.7$ GeV represent 0.014 μb/event with a resolution in $M_{\pi\pi}$ of ~0.005 GeV.

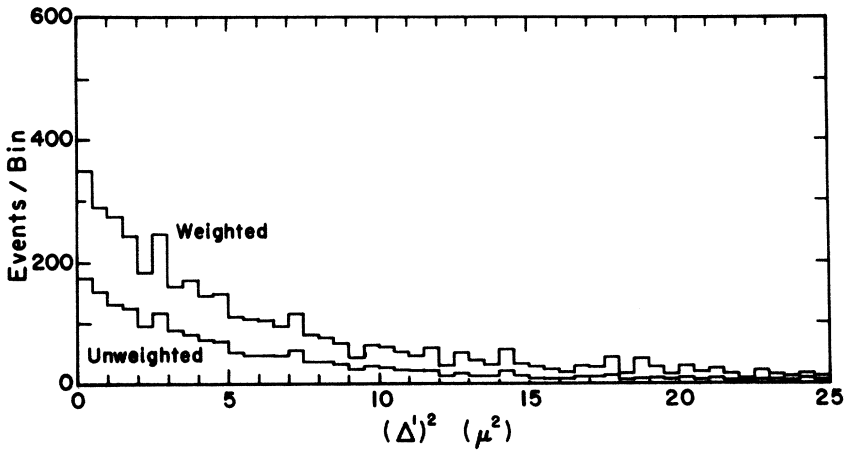

FIG. 5. The 1782 raw or 3891 weighted $\pi^+p \to \pi^+\pi^+n$ data events displayed in $(\Delta')^2$ bins of $0.5\mu^2$. The following cuts have been applied: $0.68 < MM^2 < 1.1$ GeV^2, probability ($\pi^+p \to \pi^+\pi^+n$) > twice the probability ($\pi^+p \to \pi^+p\pi^0$), and $M_{\pi\pi} < 0.7$ GeV. The weighted events with $(\Delta')^2 < 8\mu^2$ represent 0.014 μb/event with a resolution in $(\Delta')^2$ of $\sim 0.1\mu^2$.

we examined data taken with the single beam trigger and a full target. These events were visually scanned using the Varian 620i computer, which displayed them on an oscilloscope. The scanning was done to detect spurious sparks and to find interactions producing two tracks in chambers 5 or 6. A correction of 0.296 ± 0.03 was obtained for the losses due to the spark cut.

The second correction involved the actual efficiencies of the chambers combined with the criteria in CRUNCH which defined a recognizable event. The criteria for an event were (1) one beam track with at least three of the four possible sparks in the beam chambers, (2) two secondary tracks, with each track having at least three of the four possible sparks in chambers 5, 6, 7, and 8, and (3) two secondary tracks after the magnet with a total of at least three sparks in chambers 9 and 10. The efficiency of each chamber was weighted over the actual area used in gathering the data. This efficiency correction was 11.3%.

The third correction arose from erroneous reconstructions caused by missing sparks in com-

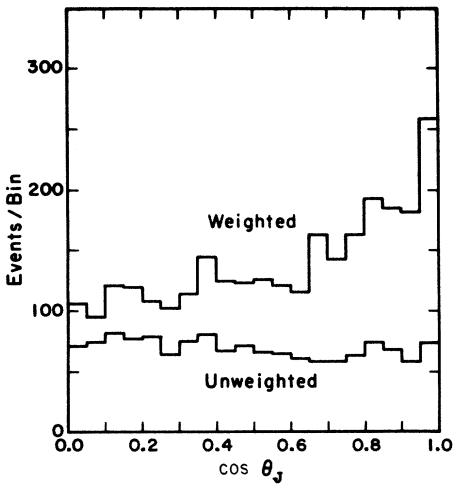

FIG. 6. The 1384 raw or 2818 weighted $\pi^+p \to \pi^+\pi^+n$ data events displayed in $\cos\theta_J$ bins of 0.05. The following cuts have been applied: $0.68 < MM^2 < 1.1$ GeV^2, probability ($\pi^+p \to \pi^+\pi^+n$) > twice the probability ($\pi^+p \to \pi^+p\pi^0$), $M_{\pi\pi} < 0.7$ GeV, and $(\Delta')^2 < 8\mu^2$. The weighted events represent 0.014 μb/event with a resolution in $\cos\theta_J$ of ~ 0.01.

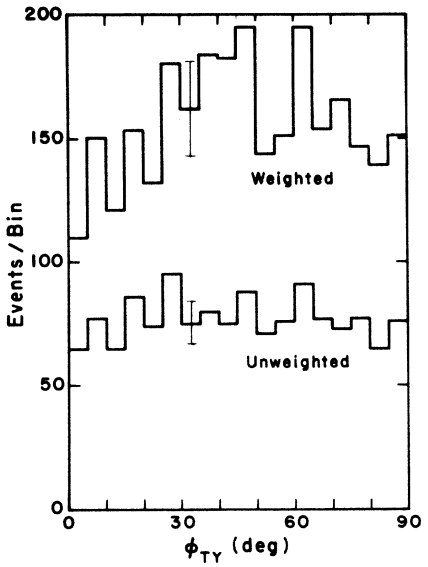

FIG. 7. The 1384 raw or 2818 weighted $\pi^+p \to \pi^+\pi^+n$ data events displayed in ϕ_{TY} bins of 5 degrees. The following cuts have been applied: $0.68 < MM^2 < 1.1$ GeV^2, probability ($\pi^+p \to \pi^+\pi^+n$) > twice the probability ($\pi^+p \to \pi^+p\pi^0$), $M_{\pi\pi} < 0.7$ GeV, and $(\Delta')^2 < 8\mu^2$. The weighted events represent 0.014 μb/event with a resolution in ϕ_{TY} of ~ 2 degrees. A typical error bar is shown.

bination with additional spurious sparks. To study this, real events with no missing sparks were modified by deleting data sparks in various combinations matching those occurring in our data. When these modified events were reconstructed by CRUNCH, incorrect tracks were found in 5.7% of the cases.

The effect of the Mylar walls of the target vessel was studied using runs taken with an empty target. Of the 5×10^7 beam pions incident on the empty vessel, 67 interacted in the Mylar walls. The X positions of their vertices, X_v, were concentrated at the ends of the target vessel and had a resolution less than 2.5 mm FWHM (full width at half maximum). The number of events with X_v inside the empty vessel was negligible. Hence, the empty target correction was minimized by retaining only those events for which X_v was less than 71.1 mm from the target center. The remaining Mylar wall correction to the target full data was ~1%. A 0.9% correction was made to compensate for absorption of beam pions in the full target. The effects of multiple and large-angle Coulomb scattering were calculated and found to be negligible.

V. RESULTS

A. Cross sections and distributions for $\pi^+p\to\pi^+\pi^+n$

Table II contains our measurements of the $\pi^+p \to \pi^+\pi^+n$ differential cross sections,

$$\frac{d^3\sigma}{dM_{\pi\pi}d(\Delta')^2\,d(\cos\theta_J)}\ ,$$

where $(\Delta')^2=\Delta^2-(\Delta^2)_{\min}$. They reflect all the corrections and weighting factors discussed in Sec. IV and were used as input for the analysis described in part C below. Essentially the same data, divided into smaller bins and integrated over $\cos\theta_J$, were used to perform the extrapolations in part B.

The projections of the data in $M_{\pi\pi}$, $(\Delta')^2$, $\cos\theta_J$, and ϕ_{TY} are given in Figs. 4 through 7. In each figure the lower histogram is a plot of the actual number of events while the upper histogram shows the data corrected by the weighting factors listed in part (a) of Table I. In order to convert the weighted data to cross sections they should be multiplied by the conversion factor 0.014 μb per weighted event as discussed in Sec. IV.

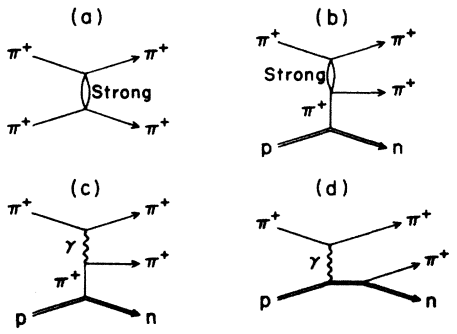

FIG. 8. Diagrams for various amplitudes discussed in the text.

B. Extrapolation to $\pi\pi\to\pi\pi$ on the mass shell

In order to use the reaction $\pi^+p\to\pi^+\pi^+n$ to obtain cross sections and phase shifts for the reaction $\pi^+\pi^+\to\pi^+\pi^+$, it is necessary to extrapolate a measured "cross section" from the region where one (virtual) pion is off the mass shell to a point on the mass shell. This is facilitated by assuming the dominance of one-pion exchange (OPE) as shown in Fig. 8(b) and then extrapolating from off-shell values of Δ^2 for the exchanged pion to the on-mass shell value of $\Delta^2=-\mu^2$. The OPE assumption is supported by the shape of the $(\Delta')^2$ distributions in Fig. 5 except near $(\Delta')^2=0$, and by the relatively flat ϕ_{TY} distributions in Fig. 7. Chew and Low[8] write the off-shell $\pi\pi$ cross section,

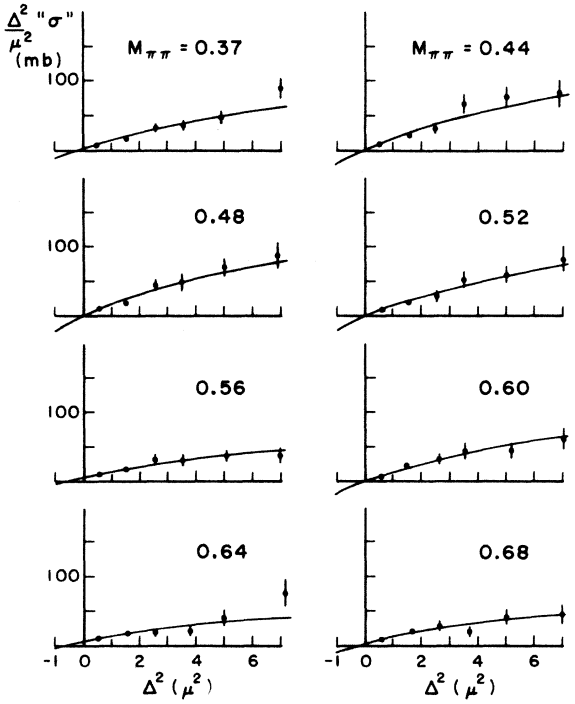

FIG. 9. Values for (Δ^2/μ^2) "σ" obtained by applying the Chew-Low equation (1) to our data. The mean value of $M_{\pi\pi}$ in GeV is indicated for each of the eight $M_{\pi\pi}$ bins shown. The curves are the results of fitting the $\alpha+\beta x$ form described in Eq. (5) of the text. Values for the curve at $\Delta^2=-1\mu^2$ and $\Delta^2=0$ as well as the χ^2 for these fits are given in Table III; results of fitting five other forms are also summarized here.

TABLE III. Summary of the $\pi^+\pi^+$ extrapolations.

$\langle M_{\pi\pi}\rangle$	Chew-Low OPE $\alpha+\beta\Delta^2$	Chew-Low OPE $\beta\Delta^2$	Chew-Low OPE $\alpha+\beta x$	(Chew-Low OPE)$\times F_{BD}$ $\alpha+\beta\Delta^2$	(Chew-Low OPE)$\times F_{BD}$ $\beta\Delta^2$	(Chew-Low OPE)$\times F_{BD}$ $\alpha+\beta x$
			$\sigma_{\pi\pi}$ (mb)			
0.37	7.5±2.1	12.7±0.8	14.1±2.8	19.6±3.4	18.9±1.3	29.4±4.4
0.44	10.3±3.2	14.8±1.2	19.2±4.3	26.7±5.2	24.0±2.0	39.2±6.8
0.48	10.1±3.5	14.6±1.1	20.9±4.7	27.9±5.7	23.6±1.9	42.2±7.6
0.52	8.4±3.5	13.3±1.1	17.8±4.6	25.8±5.7	22.0±1.8	40.7±7.6
0.56	−0.9±2.8	8.4±0.8	4.9±3.6	10.2±4.4	16.1±1.5	20.8±5.9
0.60	9.2±2.8	10.5±1.0	18.2±3.8	25.8±4.8	17.4±1.7	41.1±6.6
0.64	−0.7±3.2	8.7±0.9	3.2±4.2	6.7±4.9	15.0±1.6	13.5±6.4
0.68	2.7±2.9	8.5±0.9	8.9±3.9	14.1±4.7	15.3±1.6	25.1±6.3
			χ^2 for extrapolations			
0.37	2.7	6.9	5.8	8.7	8.8	15.5
0.44	3.6	5.7	4.9	6.9	7.2	11.7
0.48	2.8	4.5	4.4	6.5	7.1	11.6
0.52	1.2	3.4	2.3	3.8	4.3	7.8
0.56	3.7	16.4	2.4	2.0	4.1	2.5
0.60	3.2	3.4	1.1	0.6	4.2	1.1
0.64	4.0	12.9	5.5	6.4	9.5	8.5
0.68	3.5	7.9	2.8	2.7	2.8	3.1
Total/NDF	24.7/32°	61.1/40°	29.2/32°	37.6/32°	47.9/40°	61.7/32°
			Δ^2"σ" (mb) at $\Delta^2=0$			
0.37	2.5±1.3	0.0	0.9±1.3	−0.3±1.7	0.0	−2.5±1.9
0.44	2.7±1.9		0.5±2.2	−1.4±2.6		−4.1±2.9
0.48	2.8±2.1		−0.0±2.4	−2.4±3.0		−5.9±3.4
0.52	3.2±2.1		0.3±2.4	−2.1±3.1		−6.2±3.6
0.56	6.7±1.9		4.8±2.1	3.8±2.7		0.7±2.9
0.60	0.8±1.6		−1.8±1.8	−4.4±2.3		−8.5±2.8
0.64	6.6±2.2		5.2±2.4	5.3±2.9		3.6±3.3
0.68	3.9±1.9		2.1±2.1	0.8±2.7		−2.3±3.1

"σ", as

$$\frac{1}{\mu^2}\Delta^2\text{"}\sigma\text{"} = \frac{4\pi}{f^2}\frac{P_L^{\,2}}{M_{\pi\pi}}\frac{(\Delta^2+\mu^2)^2}{(M_{\pi\pi}^{\,2}-4\mu^2)^{1/2}} \times \frac{d^2\sigma(\pi^+p\to\pi^+\pi^+n)}{d\Delta^2\,dM_{\pi\pi}^{\,2}}\,, \tag{1}$$

where f^2 = twice the π^0-nucleon coupling constant $= 2\times 0.081$, and P_L is the beam momentum in the laboratory. The on-mass-shell $\pi\pi\to\pi\pi$ cross section is defined by the limit

$$\sigma_{\pi\pi} = (-1/\mu^2)\lim_{\Delta^2\to-\mu^2}(\Delta^2\text{"}\sigma\text{"})\,. \tag{2}$$

We applied (1) to our data, found the best fit of Δ^2"σ" to various functions of Δ^2, and then extrapolated each function to $\Delta^2=-\mu^2$. Three separate functional forms were investigated:

$$\Delta^2\text{"}\sigma_1\text{"} = \beta\Delta^2\,, \tag{3}$$

$$\Delta^2\text{"}\sigma_2\text{"} = \alpha+\beta\Delta^2\,, \tag{4}$$

and

$$\Delta^2\text{"}\sigma_3\text{"} = \alpha+\beta x\,, \tag{5}$$

where

$$x = (c+d\Delta^2)/(e+\Delta^2)\,; \tag{6}$$

α and β are fitted parameters. Equation (3) requires not only that $d^2\sigma(\pi^+p\to\pi^+\pi^+n)/(d\Delta^2\,dM_{\pi\pi})$ vanish at $\Delta^2=0$ but also that $(1/\Delta^2)d^2\sigma/d\Delta^2\,dM_{\pi\pi}$ be finite at $\Delta^2=0$; the forms in (4) and (5) do not have this constraint. Equation (6) is a conformal mapping which has been suggested[9-11] in order to improve the convergence of the extrapolation. The curves shown in Fig. 9 were obtained using the form (5) and are presented as an example of an unconstrained fit.

Various phenomenological form factors[12-14] have been used to modify the Chew-Low relation (1). Following the technique of Benecke and Dürr[13] we defined "σ_{BD}" = "σ" $\times F_{BD}$ where $F_{BD}(\Delta^2, M_{\pi\pi})$ = 1 at $\Delta^2=-\mu^2$. Table III summarizes the extrapolated cross sections, the goodness of the fits, and the values of Δ^2"σ" and Δ^2"σ_{BD}" at $\Delta^2=0$ obtained from the three functional forms (3), (4), and (5). Examples of on-mass-shell cross sections obtained by extrapolating (Δ^2/μ^2)"σ" are plotted in Fig. 10(a). From Table III it is apparent that the

values for the cross sections depend systematically on the choice of the functional form and the choice of a form factor, although the relative shapes are similar. The smaller errors obtained by using form (3) are due to the strong constraint at $\Delta^2 = 0$.

The $\pi\pi$ strong scattering amplitude [Fig.8(a)] can be represented by a conventional partial-wave expansion with phase shifts δ_l^I. The $I=2$ S-wave phase shift, δ_0^2, is parameterized by

$$k \cot\delta_0^2 = (1/a_2) + 0.5\, k^2 r_2 \,, \tag{7}$$

where a_2 is a scattering length, r_2 is an effective range, and $\hbar k$ is the pion momentum in the dipion rest frame. The $I=2$ D-wave phase shift, δ_2^2, is parameterized with a k^{2l+1} threshold behavior

$$\delta_2^2 = b_2 k^5 \,. \tag{8}$$

The extrapolated total cross sections, $\sigma_{\pi\pi}$, were fitted by the expression

$$\sigma_{\pi\pi} = \frac{2\times 4\pi}{k^2} \sum_{l=0,2} (2l+1) \sin^2\delta_l^2 \,. \tag{9}$$

The energy dependence of each δ_l^2 was parameterized as in (7) or (8).

These fits to the extrapolated total cross sections were insensitive to the D-wave parameter, b_2. A more sensitive method for evaluating b_2 is described in subsection C below. Anticipating the result obtained there, $b_2 = -0.0041$ F^5, we calculated the D-wave contribution to the total $\pi\pi$ cross sections presented in Table III and Fig. 10(a). By subtracting the D-wave contribution we obtained the pure S-wave contribution to the $\pi\pi$ total cross section. This allowed us to solve for the $I=2$ S-wave phase shift, δ_0^2, as a function of $M_{\pi\pi}$. The results for δ_0^2 corresponding to each of the three functional forms in Eqs. (3), (4), and (5) are presented in Fig. 10(b). The parameterization of Eq. (7) was then used to fit δ_0^2 as a function of $M_{\pi\pi}$. The best-fit values for a_2 and r_2 obtained in this fashion are listed in Table IV. The fit in part (a) of the table was made by setting $r_2 = 0$ and including only the four lowest mass points; part (b) is a two-parameter fit to all eight mass points. The fit in part (a) is more sensitive for a determination of a_2 whereas the fit in part (b) is used primarily to determine r_2.

C. $\pi\pi \to \pi\pi$ angular distributions off the mass shell

In order to obtain information on the magnitude of b_2 as well as the signs of the phase shifts, we fit the actual shapes of the $\cos\theta_J$ distributions displayed in Table II and Fig. 11. We did not extrapolate the bins in $\cos\theta_J$ to the pole $\Delta^2 = -\mu^2$ because our limited statistical accuracy would have made the extrapolation unreliable. Because the data sample for this phase of the analysis was restricted to the regions near the pole, that is, $(\Delta')^2 < 4\mu^2$, we believe that the values of a_2, b_2, and r_2 obtained from the angular distributions for $\pi^+p \to \pi^+\pi^+n$ are good approximations to the corresponding parameters for $\pi^+\pi^+ \to \pi^+\pi^+$ on mass shell.

Allowing for the symmetry of the identical particles in the final state we parameterized the total scattering amplitude for $\pi^+\pi^+ \to \pi^+\pi^+$, $F(\theta_J)$, by

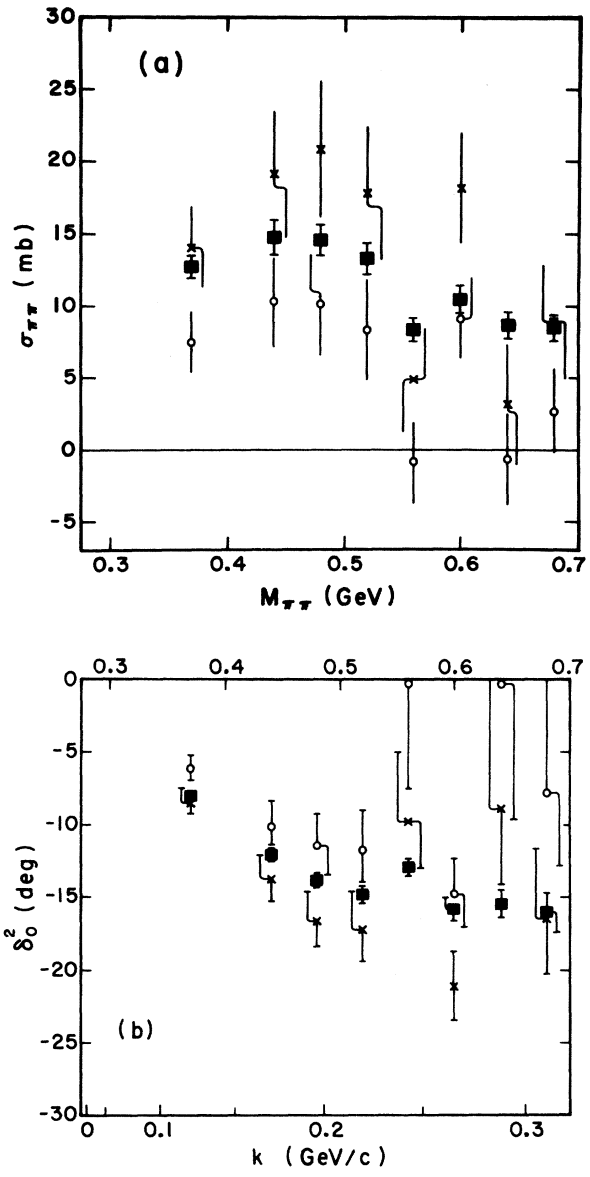

FIG. 10. (a) Extrapolated values of the elastic (total) cross section and (b) resulting $I=2$ S-wave phase shifts as a function of $M_{\pi\pi}$ for $\pi^+\pi^+ \to \pi^+\pi^+$ obtained from three functional forms. The symbol ■ is for the Δ^2"σ_1" $= \beta\Delta^2$ form, ○ is for the Δ^2"σ_2" $= \alpha + \beta\Delta^2$ form, and × is for the Δ^2"σ_3" $= \alpha + \beta x$ form.

$$F(\theta_J) = F_n(\theta_J) + F_n(\pi - \theta_J) + F_C(\theta_J) + F_C(\pi - \theta_J) , \quad (10)$$

where F_C is the Coulomb scattering amplitude and F_n is the strong-scattering amplitude given in terms of its partial-wave expansion

$$F_n(\theta_J) = \frac{1}{2ik} \sum_{I=0,2} (2l+1)[\exp(2i\delta_l^I) - 1] P_l(\cos\theta_J) . \quad (11)$$

In the expression for F_n, $\hbar k$ was taken to be the momentum of a pion in the final-state dipion system and the phase shifts were parameterized as in Eqs. (7) and (8). The differential angular distribution for our folded distribution from $0 \leq \cos\theta_J \leq 1$ is given by

$$d\sigma_{\pi\pi}/d\Omega(\theta_J) = |F(\theta_J)|^2 . \quad (12)$$

We investigated the possibility of determining the signs of the phase shifts by fitting this angular distribution and studying its dependence on the interference between F_C and F_n.

In a preliminary analysis[15] we wrote the amplitude for the $\pi^+\pi^+ \to \pi^+\pi^+$ interaction using only contributions from Figs. 8(b) and 8(c). The off-mass-shell Coulomb amplitude obtained from Fig. 8(c) has $1/t$ dependence and its interference with the strong amplitude has a significant effect on the total amplitude off the mass shell. However, this Coulomb amplitude is not gauge-invariant. Michael[16] has suggested that in order to have a gauge-invariant Coulomb amplitude off the mass shell, at least the diagram in Fig. 8(d) must be added to the Coulomb diagram in Fig. 8(c). The effect of adding these two diagrams is to change the $1/t$ pole behavior to an approximately $1/\sqrt{t}$ behavior for the Coulomb amplitude off the mass shell. This considerably reduces the Coulomb amplitude and its interference effects.

In our final analysis we have used a gauge-invariant form[17] of the Coulomb amplitude which includes not only the diagrams in Figs. 8(c) and 8(d), but all diagrams needed to treat the radiative corrections for this problem. Thus we considered, for example, the diagrams with a virtual photon connecting pairs of the external legs in Fig. 8(b). The inclusion of radiative corrections modifies the form of Eq. (10) to read

$$F(\theta_J) = [F_n(\theta_J) + F_n(\pi - \theta_J) + f_C(\theta_J)\, e^{i\phi} + f_C(\pi - \theta_J)\, e^{i\psi}]\, e^{\delta} , \quad (13)$$

where $f_C(\theta_J)$ is the amplitude from Figs. 8(c) and 8(d). The real part of the radiative correction is given by δ and the imaginary parts of the radiative correction are given by ϕ and ψ. The imaginary parts provide the relative phases and hence the interference effects between the purely strong amplitude and the various terms of the Coulomb amplitude. They have been found to be negligible unless the dipion mass is very near threshold, that is, the center-of-mass momentum of the di-

TABLE IV. Parameters of the best fits to the δ_0^2 phase shifts shown in Fig. 10(b).

(a)

Using the four lowest mass points to determine a_2 with $r_2 = 0$

For "σ_1":	$a_2 = -0.24 \pm 0.01$ F
For "σ_2":	$a_2 = -0.20 \pm 0.02$ F
For "σ_3":	$a_2 = -0.27 \pm 0.03$ F

(b)

Using all eight mass points to determine both a_2 and r_2

For "σ_1":	$a_2 = -0.25^{+0.02}_{-0.03}$ F	$r_2 = -1.0 \pm 0.3$ F
For "σ_2":	$a_2 = -0.22^{+0.06}_{-0.12}$ F	$r_2 = -1.5^{+3.7}_{-3.0}$ F
For "σ_3":	$a_2 = -0.28^{+0.06}_{-0.08}$ F	$r_2 = -0.5^{+1.0}_{-1.7}$ F

(c)

Average of the a_2 and r_2 determinations

$a_2 = -0.24 \pm 0.02$ F $\qquad r_2 = -1.0 \pm 1.7$ F

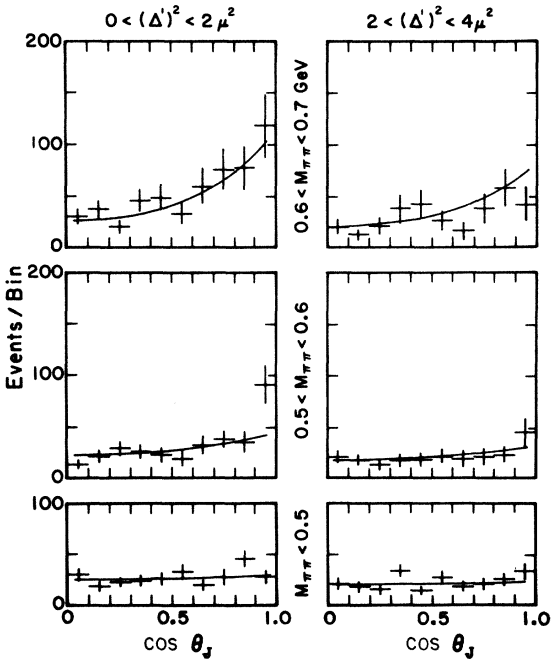

FIG. 11. The off-shell $\cos\theta_J$ distributions for the $\pi^+p \to \pi^+\pi^+n$ data weighted by the factors in Table I(a). The data are displayed in $\cos\theta_J$ bins of 0.1. The cuts on $M_{\pi\pi}$ and Δ^2 for each plot are indicated on the figure. The curves are for the fit to the data using a gauge-invariant Coulomb amplitude described in Sec. V C.

pion system is less than 5 MeV/c. Thus, considering our statistical accuracy and resolution we neglected the imaginary parts of the radiative correction. However, we have included the real radiative correction. This correction, the gauge-invariant Coulomb-Born amplitude, and the parameterizations in Eqs. (7) and (8) were used to obtain the $\pi^+p \to \pi^+\pi^+n$ cross section. The details of this calculation are given in Ref. 17. The Δ^2 dependences of the strong amplitude as well as the Coulomb amplitude were used explicitly in obtaining a fit to the cross sections listed in Table II. The best fit was

$$a_2 = -0.22^{+}_{-}{}^{.03}_{.04}\ \mathrm{F} = (-0.16^{+}_{-}{}^{.02}_{.03})\mu^{-1},$$

$$r_2 = -0.34^{+0.9}_{-1.2}\ \mathrm{F} = (-0.24^{+0.64}_{-0.87})\mu^{-1},$$

$$b_2 = -0.0041^{+}_{-}{}^{.0025}_{.0021}\ \mathrm{F}^5 = (-0.0007 \pm 0.0004)\mu^{-5}$$

and gave a χ^2 of 57 for 57 degrees of freedom. Figure 11 shows the $\cos\theta_J$ dependence of the above fit. The fit clearly shows that a_2 and b_2 (as well as r_2) have the same signs but does not distinguish between the first and third quadrants. No fit was possible in the other two quadrants. Thus with the gauge-invariant Coulomb amplitude we are unable to determine the signs of the $I=2$ phase shifts from their interference with the Coulomb amplitude. The signs quoted ($a_2<0$ and $b_2<0$) are those anticipated on the basis of a preliminary analysis of a companion experiment ($\pi^-p \to \pi^+\pi^-n$) done with the same experimental apparatus. Our results for a_2 from Secs. V B and V C are inconsistent with a number of theoretical calculations[18-22] which predict a value of $a_2 \sim -0.06\mu^{-1}$. As we have determined in subsection B, inclusion of conformal mapping, or form factors, or both, in the fitting process makes our $\sigma_{\pi\pi}$'s even larger and hence would make our value of $|a_2|$ larger, giving an even greater discrepancy with these theories. Other experimental results[23-33] are consistent with δ_0^2's (and hence values of a_2) whose magnitudes are larger than the theoretical value. A comparison of our experimental results for δ_0^2 with other published phase shift results is shown in Fig. 12.

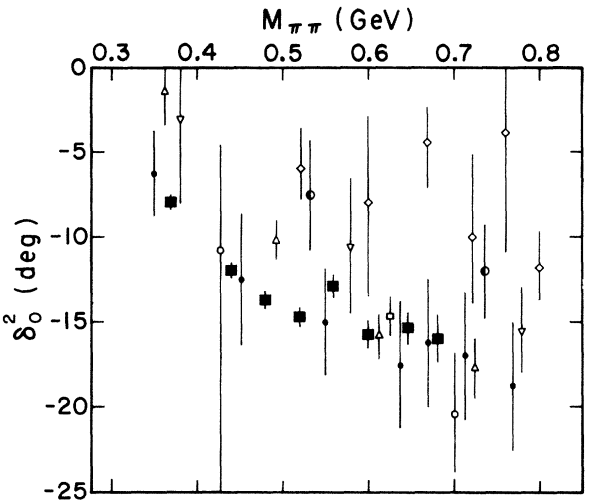

FIG. 12. Our data from this experiment (■) for $I=2$ S-wave phase shifts as a function of $M_{\pi\pi}$ compared with some previously published data: ◇ Baton *et al.* (Ref. 27); ● Walker *et al.* (Ref. 24); ○ Biswas *et al.* (Ref. 25); △ Colton *et al.* (Ref. 28); ▽ Cohen *et al.* (Ref. 31); ◐ Durusoy *et al.* (Ref. 32); and □ Hoogland *et al.* (Ref. 33).

ACKNOWLEDGMENTS

We wish to thank Dr. Jerome Helland, John Meyers, and Dr. Victor Bierman for their efforts in the initial states of the experiment, and George Theodosiou for help during the runs; William Rickhoff and Ron Erichsen for their aid in the construction and data-taking stages; Alex Horvath and the staff of the Notre Dame machine shop especially for the construction of the magnetostrictive wire spark chambers; and Dr. Bruce Cork and the Argonne ZGS staff, especially Chester Brzegowy. During the analysis phase much assistance was given by Dr. Vatsala Srinivasan, Dr. Paul Kirk, our colleagues at Michigan State University, and Brian Walsh and the staff of the Notre Dame Computing Center. We wish to thank the following for their contributions to our understanding and analysis of this experiment: the theorists at Notre Dame, especially Dr. James Cushing, Dr. Walter Johnson, and Dr. Paul DeCelles; also Dr. Paul Tsai and Dr. Sydney Drell from SLAC.

*Research supported in part by the National Science Foundation.

†Work supported by the United States Atomic Energy Commission.

[1]H. Wind, Nucl. Instrum. Methods 84, 117 (1970).

[2]V. L. Highland and R. J. Macek, Nucl. Instrum. Methods 64, 69 (1968).

[3]D. L. Parker, Michigan State University, private communication.

[4]D. E. Fries, SLAC Report No. SLAC-99, 1969 (unpublished).

[5]I. Derado and R. Leedy, SLAC Report No. SLAC-72, 1967 (unpublished).

[6]Thanks must be extended to our collaborators at Michigan State University for suggesting this approach to solving the geometrical weighting problem.

[7]J. W. Lamsa, doctoral thesis, University of Notre Dame, 1966 (unpublished).

[8]G. F. Chew and F. E. Low, Phys. Rev. 113, 1640 (1959).

[9]J. P. Baton, G. Laurens, and J. Reignier, Phys. Lett. 33B, 525 (1970).
[10]R. E. Cutkosky and B. B. Deo, Phys. Rev. 174, 1859 (1968).
[11]S. Ciulli, Nuovo Cimento 61A, 787 (1969); 62A, 301 (1969).
[12]H. P. Dürr and H. Pilkuhn, Nuovo Cimento 40A, 899 (1965).
[13]J. Benecke and H. P. Dürr, Nuovo Cimento 56A, 269 (1968).
[14]G. Wolf, Phys. Rev. 182, 1538 (1969).
[15]J. A. Poirier, in *Proceedings of the XVI International Conference on High Energy Physics, Chicago-Batavia, Ill., 1972,* edited by J. D. Jackson and A. Roberts (NAL, Batavia, Ill, 1973), Vol. 1, p. 9.
[16]C. Michael, Nucl. Phys. B61, 199 (1973).
[17]C-j. Chen and J. T. Cushing, Phys. Rev. D 10, 113 (1974).
[18]S. Weinberg, Phys. Rev. Lett. 17, 616 (1966).
[19]J. R. Fulco and D. Y. Wong, Phys. Rev. Lett. 19, 1399 (1967).
[20]R. Arnowitt, M. H. Friedman, P. Nath, and R. Suitor, Phys. Rev. Lett. 20, 475 (1968); Phys. Rev. 175, 1820 (1968).
[21]C. Lovelace, Phys. Lett. 28B, 264 (1968); in *Proceedings of the Conference on $\pi\pi$ and $K\pi$ Interactions, Argonne National Laboratory, 1969,* edited by F. Loeffler and E. D. Malamud (Argonne National Laboratory, Argonne, Ill., 1969), p. 562.
[22]H. J. Schnitzer, Phys. Rev. D 2, 1621 (1970).
[23]N. Armenise, B. Ghidini, S. Mongelli, A. Romano, P. Waloschek, J. Laberrigue-Frolow, Nguyen Hun Khanh, C. Ouannes, M. Sene, and L. Vigneron, Nuovo Cimento 37, 361 (1965) ($\pi^+p \to n\pi^+\pi^+$ at 2.75 GeV/c).
[24]W. D. Walker, J. Carroll, A. Garfinkel, and B. Y. Oh, Phys. Rev. Lett. 18, 630 (1967) (a compilation of $\pi^+{}^-p \to \pi^+\pi^+{}^-{}^0p$ or n at 2, 3, and 7 GeV/c).
[25]N. N. Biswas, N. M. Cason, P. B. Johnson, V. P. Kenney, J. A. Poirier, W. D. Shephard, and R. Torgerson, Phys. Lett. 27B, 513 (1968) (a compilation of $\pi^-p \to \pi^-\pi^-\Delta^{++}$ at 3.2 and 4.2 GeV/c).
[26]G. V. Beketov, S. M. Zombkovskiı, A. B. Kaĭdalov, B. S. Konovalov, S. P. Kruchinin, Ya. M. Selektor, and V. N. Sulyachenko, Yad. Fiz. 12, 112 (1970). [Sov. J. Nucl. Phys. 12, 62 (1971)] ($\pi^-p \to \pi^-\pi^-\Delta^{++}$ at 4.45 GeV/c).
[27]J. P. Baton, G. Laurens, and J. Reignier, Phys. Lett. 33B, 525 and 528 (1970) ($\pi^-p \to \pi^+\pi^-n$ at 2.77 GeV/c).
[28]E. Colton, E. Malamud, P. E. Schlein, A. D. Johnson, V. J. Stenger, and P. G. Wohlmut, Phys. Rev. D 3, 2028 (1971) ($\pi^-p \to \pi^-\pi^-\Delta^{++}$ from 2.7 to 4.2 GeV/c).
[29]L. J. Gutay, in Proceedings Zero Gradient Synchrotron Workshops, 1971, Argonne National Laboratory Report No. ANL/HEP-7208, Vol. I, p. 58 (unpublished).
[30]R. D. Baker, paper No. 426 submitted to the XVI International Conference on High Energy Physics at Chicago-Batavia, Ill., 1972 (unpublished) ($\pi^+p \to \pi^+\pi^+n$ at 1.4 and 1.5 GeV/c).
[31]D. Cohen, T. Ferbel, P. Slattery, and B. Werner, Phys. Rev. D 7, 661 (1973) ($\pi^-d \to \pi^-\pi^-pp$ at 7 GeV/c).
[32]N. B. Durusoy, M. Baubillier, R. George, M. Goldberg, A. M. Touchard, N. Armenise, M. T. Fogli-Muciaccia, and A. Silvestri, Phys. Lett. 45B, 517 (1973) ($\pi^-d \to \pi^-\pi^-pp$ at 9 GeV/c).
[33]W. Hoogland, G. Grayer, B. Hyams, C. Jones, P. Weilhammer, W. Blum, H. Dietl, W. Koch, E. Lorenz, G. Lütjens, W. Männer, J. Meissburger, and U. Stierlin, Nucl. Phys. B69, 266 (1974) ($\pi^+p \to \pi^+\pi^+n$ at 12.5 GeV/c).